LBNL-40866

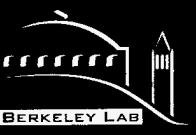

ERNEST ORLANDO LAWRENCE
BERKELEY NATIONAL LABORATORY

Monte Carlo Simulations of Neutron Well-Logging in Granite and Sand to Detect Water and Trichloroethane (TCA)

D.D. Hua, R.J. Donahue, C.M. Celata,
and E. Greenspan

Environment, Health and Safety Division

January 1998

LBNL-40866
UC-400

Monte Carlo Simulations of Neutron Well-Logging in Granite and Sand to Detect Water and Trichloroethane (TCA)

D.D. Hua, R.J. Donahue, C.M. Celata, and E. Greenspan

Environment, Health and Safety Division
Ernest Orlando Lawrence Berkeley National Laboratory
University of California
Berkeley, California 94720

January 1998

This work was supported by the U.S. Department of Energy under Contract No. DE-AC03-76SF00098.

Monte Carlo Simulations of Neutron Well-Logging in Granite and Sand to Detect Water and Trichloroethane (TCA)

D. D. Hua,[1,2] R. J. Donahue,[1] C. M. Celata[1] and E. Greenspan[2]

[1]Ernest Orlando Lawrence Berkeley National Laboratory
[2]Department of Nuclear Engineering
University of California
Berkeley, CA 94720

Abstract

The Monte Carlo code MCNP [1] is used in simulations of neutron well-logging in granite to detect water and TCA ($C_2H_3Cl_3$), a common ground contaminant, in fractures of 1 cm and 1 mm thickness at various distances and orientations. Also simulated is neutron well-logging in wet sand to detect TCA and lead (Pb) at various uniform concentrations. The ^{3}H(d,n) (DT) and ^{2}H(d,n) (DD) neutron producing reactions are used in the simulations to assess the relative performance of each. Simulations are also performed to determine the efficiency of several detector materials such as CdZnTe, Ge and NaI as a function of photon energy. Results indicate that, by examining the signal from the 6.11 MeV gamma from the thermal neutron capture of Cl in TCA, trace amounts (few ppm) are detectable in saline-free media. Water and TCA filled fractures are also detectable. These results are summarized in Tables 7-21. Motivation for this work is based on the need for detection of trace environmental pollutants as well as possible fracture characterization of geologic media.

1 Introduction

A typical neutron well-logging experiment begins with the release of a pulse of neutrons, which for our purposes are either 14 MeV or 2.45 MeV neutrons generated from ^{3}H(d,n) (referred to as DT neutrons) or ^{2}H(d,n) (referred to as DD neutrons) fusion reactions respectively. A photon detector is used to measure photons produced via the interactions of neutrons with various nuclei of the medium. In particular, we are interested in obtaining the photon spectrum due to absorption of thermal neutrons ($\sim 10^{-2}\ eV$), where each nucleus, after capturing a thermal neutron, emits a distinct and discrete set of photon energy lines. For simulations involving water, we are interested in detecting the 2.23 MeV photon line from thermal neutron capture in H. For the case of TCA, the 6.11 MeV line from Cl [2, 3, 4] is of greatest interest since it has a very large thermal neutron capture cross section and will therefore produce a large signal.

For the purpose of selecting an optimal neutron source for well-logging, we use both DT and DD neutrons in our simulations. DT neutrons are produced from readily available commercial accelerator-based neutron tubes, but at 14 MeV, these neutrons go through many scatterings before being thermalized. In the thermalization process, many of the fast neutrons are inelastically scattered on nuclei, producing many photons that could obscure photon signals from thermal neutron capture. The total neutron absorption cross section rises above a few MeV resulting in significant loss of neutron flux. In addition, DT accelerators contain radioactive tritium, which poses a potential safety containment problem. In contrast, DD reactions do not require radioactive target nuclei and their neutrons, produced at 2.45 MeV, are below many high-energy inelastic resonances and so undergo fewer scatterings before being thermalized. The total absorption cross section is approximately a factor of 100 lower in the energy range of a few MeV than at 14 MeV. Thus, more DD than DT neutrons survive to become thermal neutrons, and be captured by nuclei to emit the desired characteristic photons. DD reactions however produce fewer neutrons than DT reactions due to a lower reaction cross section, since $\sigma_{DD} \ll \sigma_{DT}$, see Fig. 1.

The second component needed in well-logging applications is the photon detector. Conventional detectors such as scintillators, which could operate at room temperature but have poor energy resolution, while Germanium detectors, which have excellent energy resolution,

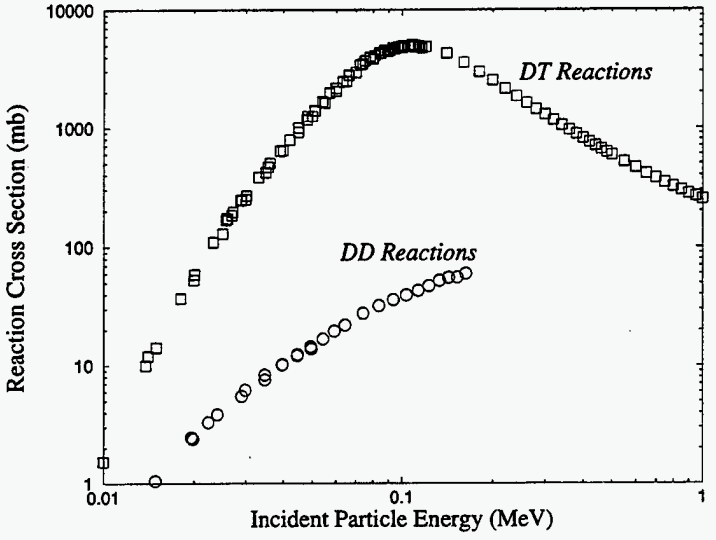

Figure 1: DT and DD reaction cross sections versus incident deuteron energy.

must be operated near liquid nitrogen temperature. In contrast, high-Z semiconductors like CdZnTe detectors have better energy resolution than scintillators (though not as good as that of germanium detectors) and can be operated at room temperature, making it particularly suited to field applications such as ours.

The organization of the paper is as follows. In Section 2, we introduce the geometry and materials used in the well-logging simulations. In Section 3, we discuss the MCNP tally used in the simulations, including the need for time-gating and cell-biasing. In Section 4, we compare the efficiency and energy resolution of various detector materials and volumes. In Section 5, we present the results of the simulations: Section 5.1 presents results of attempts to detect water in 1 cm and 1 mm-fractures in dry and wet granite, using DT neutrons; Also in Section 5.1 are results for salt water in 1 cm and 1 mm-fractures of salt water, and TCA in dry and wet granite, using DT neutrons (DD neutrons for one case only); in addition, results of uniform concentrations of TCA's and Pb in wet sand using DT neutrons are presented: Section 5.2 presents results of 1-mm fractures containing salt water in dry granite, with angular collimation in order to try to localize the position of the fracture. Lastly, Section 6 summarizes results and conclusions.

Table 1: Molecular Composition of Granite and Sand

Molecules	Granite (%)	Sand (%)
SiO_2	66.090	72
Al_2O_3	15.730	15
CaO	3.830	1
Na_2O	3.750	3
K_2O	2.730	2
FeO	2.730	3
MgO	1.740	1
Fe_2O_3	1.380	2
H_2O	1.040	-
TiO_2	0.540	-
P_2O_5	0.180	-
MnO	0.008	-
CO_2	0.008	1

2 Geometry

The media used in the simulations are either granite,[1] wet granite (granite with 0.1 g/cc^3 water in pore space) or wet sand (sand with $\sim 30\%$ water). Their molecular compositions are listed in Table 1. These choices reflect the conditions under which detailed characterization of fractured media or minimum detectable contaminant levels are needed.

Fig. 2 depicts the x-y ($z = 0$) plane of a typical geometry model in our simulations. The medium is a cube of length 174 cm, where $-87cm \leq x, y, z \leq 87cm$. This dimension is such that the majority of neutrons released from a source (located at $(0, 0, 4cm)$, roughly the center of the cube) are absorbed before escaping across the cubical boundary surface. The neutron source is a point isotropic source. A cylindrical borehole of radius 5 cm along the z-axis is cut out of the medium. At the origin is a Cd-sphere ($\rho = 2.58\ g/cc$) of radius 2 cm, covered by 0.5 cm thickness of B_4C neutron shield ($\rho = 2.255\ g/cc$).

[1]Note that granite itself contains a small amount of water

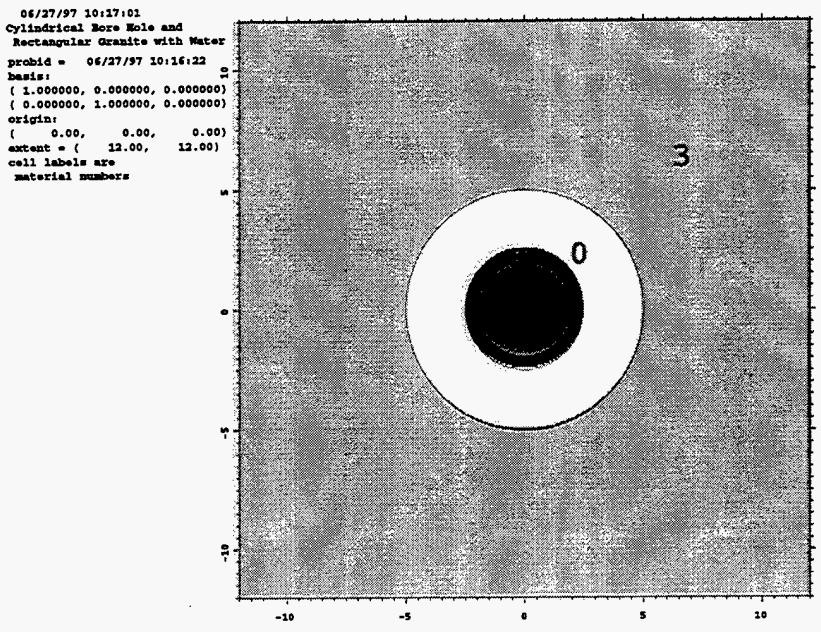

Figure 2: The $z = 0$ plane of a typical simulation geometry (units in cm): Region 0 is the 10 cm diameter cylindrical borehole, Region 1 (innermost region) the 0.5 cm thick spherical Cd detector, Region 2 (second concentric region) the 4 cm diameter B_4C neutron shield and Region 3 (partially shown) the medium, approximately 5.3 m^3 volume. The detector and B_4C detector shield are centered within the borehole.

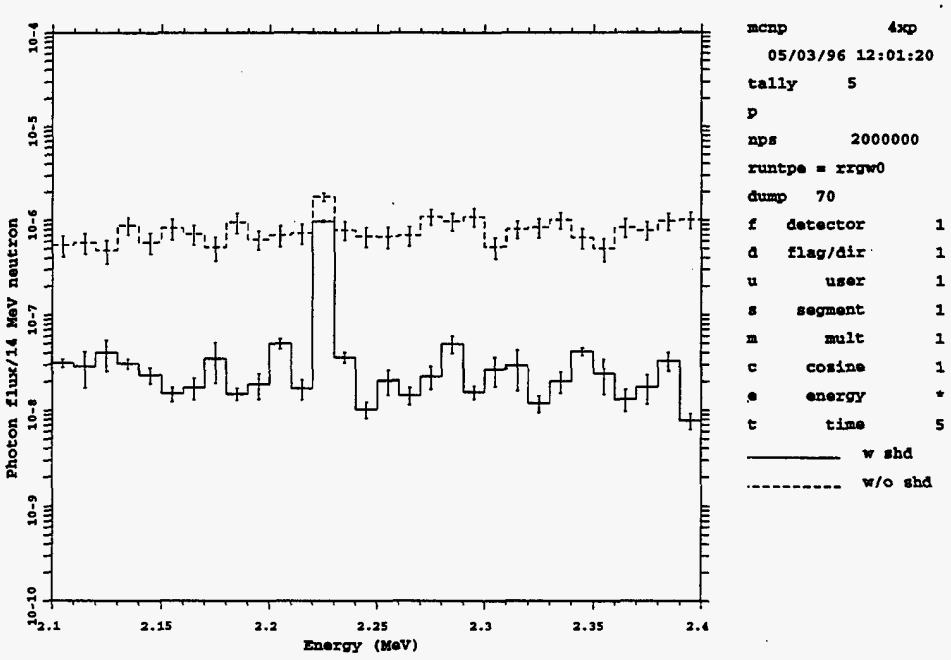

Figure 3: Photon Tally (n/cm^2/source neutron) for a B_4C-shielded detector (solid lines) and an unshielded detector (dashed lines).

It is necessary to shield the Cadmium in the detector from thermal neutron interactions because of it's large thermal neutron capture cross section. Such interactions could swamp the detector with the associated photons produced in thermal neutron capture. The B_4C region shields the detector from thermal neutron interaction, which minimizes radiation damage and reduces unwanted photon production in the detector, by taking advantage of the large Boron cross section at low neutron energies ($\sim$ 3800 barns at thermal energies). The following figure illustrates the necessity of providing thermal neutron shielding for the Cadmium in the detector. Fig. 3 compares photon spectra from a DT neutron source for two cases: for a Cd-shielded detector (solid line), and an unshielded detector (dashed line). The 2.23 MeV photon signal from Hydrogen capture is clearly seen above the background for the shielded detector, whereas the signal is obscured by the background for the unshielded detector.

3 Tally Statistics and Detector Response

3.1 Tallies and Time-gating

Fig. 4 is an MCNP plot of the total neutron absorption cross section (solid curve) which include (n,γ) cross section (dashed curve) for granite. The total neutron cross section (which includes elastic scattering, inelastic scattering, absorption, etc.) varies between 1 and 10 barns over this energy range. From this one can see that complete neutron absorption is much more likely to occur with a 14 MeV DD neutron source than with a 2.45 MeV DD neutron source. In the energy range of 10 to 14 MeV absorption reactions account for about 1/3 to 1/2 of the total cross section, whereas in the 2 to 3 MeV energy range absorption acounts for less than 1% of the total cross section. This makes DD-produced neutrons a more efficient source of thermal neutrons than DT-produced neutrons - per source neutron. However one must weigh this against the difference in the DD vs DT reaction cross section as discussed earlier. These arguments provide some incentive to perform some comparisons between DD and DT sources for otherwise identical models. These will be presented in the Results section.

In sand and granite media photons produced from inelastic (n,n') interactions, with Compton down-scatterings, could increase the background so much that the spectrum due to thermal neutron capture is obscured. Fortunately, these inelastic interactions take place relatively quickly after the release of DT neutrons. After a few μsec, most of the fast neutrons will have been either thermalized or absorbed, and thus most of the photons produced subsequently are from thermal neutron capture. This makes possible the common technique of gating off the detector for an initial time period after the neutron source is pulsed to reduce the background and prevent pulse pileup of extraneous signals. Fig. 5 is a plot of the total photon tallies (over all photon energies) versus time for dry and wet granite media. From $t = 0$ *sec* to $t = 10^{-8}$ *sec*, the photon flux at the detector is quite high, 1.42×10^{-3} $cm^{-2}sec^{-1}$, due to inelastic neutron scatterings. This results in a large background. Also plotted is the 2.23 MeV photon flux, once again showing the high flux, immediately after the neutron pulse, due to inelastic scattering. However 2.23 MeV photon fluxes from *thermal neutron capture* by H arrive in the neighborhood of 1 μsec and increase to a maximum at 200 - 500 μsec, decreasing to zero after 10^{-2} *sec*. The total photon flux

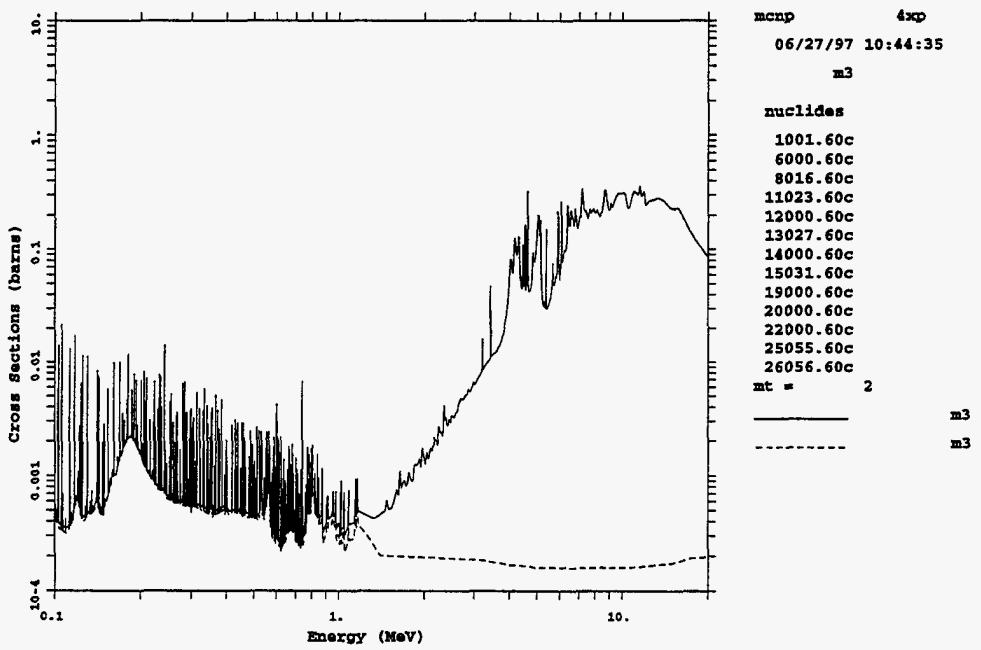

Figure 4: Neutron total absorption (solid curve) and (n,γ) (dashed curve) cross sections for granite.

starts to increase at 20 μsec and subsequently follows the trend of the 2.23 MeV flux, which suggests that all the flux from 20 μsec onward is due to thermal neutron capture. For the wet granite medium, there is significantly more H in the medium (0.1 g/cc water) than in dry granite to thermalize neutrons. The higher concentration of H also results in enhanced probability of thermal neutron capture. Hence the 2.23 MeV flux from the wet granite case arrives earlier and is larger than that from dry granite. It is interesting to note that the presence of small amounts of water in the medium does not affect the thermalizing time, but only the magnitude of the thermalized neutron flux.

The significant reduction in background photon flux when the detector is gated off for 30 μsec after the neutron pulse is shown in Fig. 6. These results are shown for illustrative purposes only. DT neutrons are released in a granite medium containing a nearby water-filled fracture. The goal is to detect water in the fracture by looking for the 2.23 MeV line resulting from thermal neutron capture in H. The dashed lines represent photon spectra from a detector tallying from $t = 0$ to $t = \infty$. The signal at 2.23 MeV is not distinguishable from background. In contrast, the solid lines representing photon spectra tallied from $t = 30$ μs to $t = \infty$ show a signal that is an order of magnitude above background. It is

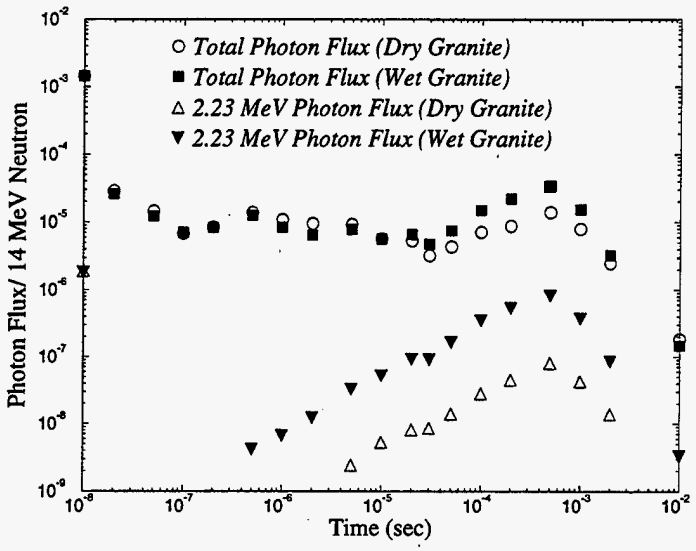

Figure 5: Photon tallies for dry and wet granite medium

clear that time-gating the detector yields a higher signal-to-noise ratio at 2.23 MeV. An important additional advantage is that the time-gated background is an order of magnitude lower than the non time-gated background. This is an advantage due to the pulse pileup limitations of most detector systems.

The F5 tally from MCNP [1] is used in all the simulations due to its good statistical properties. The F5 tally, also known as the point detector tally, is a deterministic estimate of the photon flux at a spatial point. In this work the tally is placed at the center of the spherical Cd detector. This tally makes an estimate of the flux at this point from collision events throughout the problem. These contributions are added to the final result but with a weight reduced by the probability of the particle travelling from the collision point to the tally point. This results in many small contributions to the resulting flux value yielding a better statistical estimate. The photon spectrum (see Figs. 3 and 6) is a plot of the photon tally, interpreted as the photon flux (n/cm^2/source-neutron) that reaches the detector, versus photon energy in intervals of 10^4 eV. The majority of simulations use 2×10^6 source neutron histories to produce acceptably small error bars.

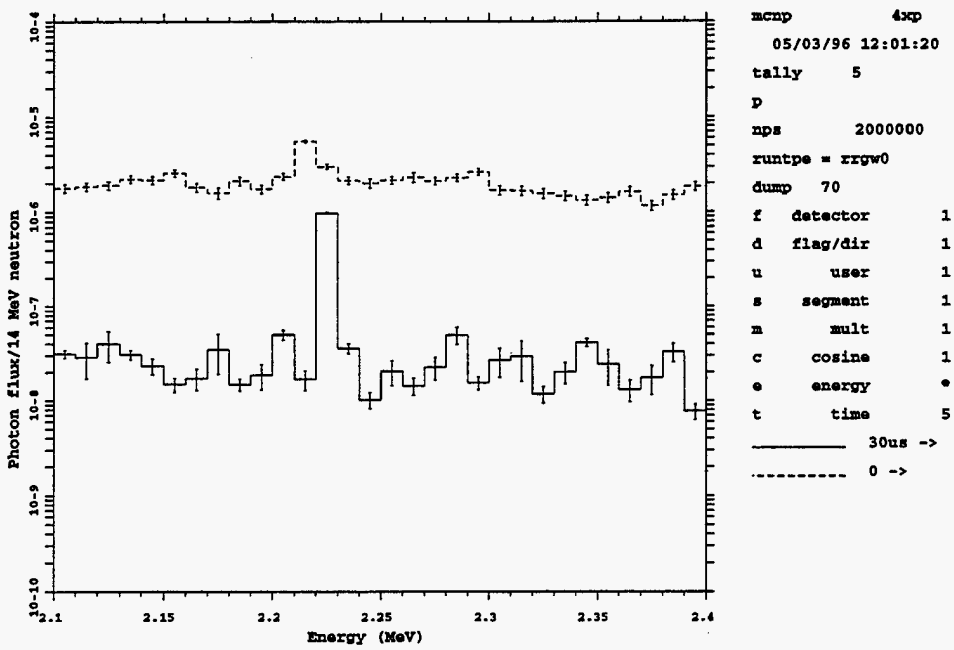

Figure 6: Illustration of photon tally time intervals for granite with a nearby water-filled fracture. Solid curve has tally time from 30 μs to ∞. Dashed curve has tally time from 0 to ∞.

3.2 Cell Biasing

Due to the large dimension used in the simulations, a cube with sides of 154 *cm*, many source neutrons are needed to ensure statistical reliability and so MCNP computation time was quite high, usually requiring a few days on a Sun SPARC10 workstation. Hence cell biasing [1], a numerical and statistical method to count those neutrons and photons in regions of interest (i.e. near the detector) relatively more than those in far away regions, was used to reduce computation time. The relative weights of different cells, constructed as nested cubes, are obtained using the SWAN [5] code, a deterministic (as opposed to Monte Carlo) neutron and photon transport code. The cell weights used in MCNP correspond to SWAN results which determined the relative importance of various regions in contributing to the photon flux at the detector. Appendix A.2 contains a sample MCNP input code with cell biasing.

4 Efficiency and Energy Resolution of Detectors

The efficiency of a detector determines the number of incoming photons that are counted, and thus has a big influence on the statistical reliability of the gathered data. Detectors with low efficiency may require higher source neutron intensity (number of source neutron released per second) and larger volume to gather enough data. Table 2 lists detector efficiencies as a function of detector volume and photon energy for detector materials Cd_9ZnTe_{10}, Ge(Li) and NaI. These efficiencies are calculated using MCNP with it's pulse height tally option. The MCNP pulse height tally records the energy deposited in a cell by each source particle and its secondary particles. This results in a realistic modeling of microscopic events. A planar mono-energetic photon source is assumed to be at normal incidence with respect to one surface of a cubic detector. The detector efficiency (photopeak counts per incident photon) is determined as a function of the incident photon energy and the detector volume.

These results demonstrate one of the advantages of the Cd_9ZnTe_{10} detector - for a fixed volume it has a higher efficiency than either Ge(Li) or NaI. For example, at 2 MeV and for 10 cc's, Cd_9ZnTe_{10} has an efficiency roughly a factor of 2.5 higher than either Ge(Li) or NaI. At 6 MeV the efficiency of Cd_9ZnTe_{10} is higher by a factor of roughly 3. Based on these advantages the detector is treated as Cd_9ZnTe_{10}.

Another concern is the energy resolution of a detector, which reflects the ability to distinguish a photon energy peak from that of neighboring peaks. Poor energy resolution can result in, for example, an increased threshold for detecting trace contaminants in the media due to the inability to distinguish the photon energy peak of a contaminant from the background signal. In Fig. 7 plots of photon flux versus photon energy from MCNP runs for two cases are shown: (1) a wet sand medium (see Table 1 for its molecular composition) and (2) a uniform concentration of TCA at 100 ppm in a wet sand medium. The signal from the case with TCA, the photon flux at 6.11 MeV due to Cl thermal neutron capture, is clearly visible above the background (wet sand medium) if the energy resolution is 0.01 MeV, corresponding to 0.16%. However, if the energy resolution is 3%, then the photon fluxes from 6 MeV to 6.05 MeV are included, and the signal is somewhat obscured. Table 3 lists photon fluxes for the TCA and the background cases as a function of energy resolution about the 6.11 MeV energy interval. The Cl signal drops from being 7.1 times above

Table 2: Detector efficiency (in %) versus detector volume (rows) for various incident photon energy (columns).

Detector Material - Cd_9ZnTe_{10}								
	0.1 MeV	0.5 MeV	1 MeV	2 MeV	4 MeV	6 MeV	8 MeV	10 MeV
1 cc	95.7	14.6	4.58	1.58	5.11E-1	2.35E-1	1.08E-1	5.46E-2
2 cc	98.7	18.2	6.10	2.31	7.74E-1	3.60E-1	1.86E-1	9.77E-2
5 cc	99.0	23.8	8.82	3.62	1.33	6.68E-1	3.67E-1	2.25E-1
10 cc	99.2	29.0	11.6	5.03	2.01	1.08	6.28E-1	4.09E-1
20 cc	99.4	35.1	15.2	7.00	3.02	1.73	1.07	7.40E-1
50 cc	99.6	54.5	28.4	14.7	7.22	4.69	3.24	2.38
80 cc	96.9	60.5	33.9	18.4	9.78	6.55	4.77	3.60

Detector Material - Ge(Li)								
	0.1 MeV	0.5 MeV	1 MeV	2 MeV	4 MeV	6 MeV	8 MeV	10 MeV
1 cc	83.6	3.83	1.10	4.19E-1	1.35E-1	6.24E-2	3.02E-2	1.34E-2
2 cc	88.1	5.16	1.64	6.23E-1	2.17E-1	9.72E-2	4.78E-2	2.28E-2
5 cc	92.2	7.69	2.74	1.13	4.07E-1	1.89E-1	9.43E-2	4.77E-2
10 cc	94.5	10.5	4.07	1.77	6.69E-1	3.23E-1	1.65E-1	8.82E-2
20 cc	96.1	14.3	6.00	2.74	1.09	5.62E-1	2.99E-1	1.74E -1
50 cc	97.6	25.7	12.5	6.53	2.97	1.71	1.00	6.55E-1
80 cc	95.6	30.9	16.2	8.86	4.28	2.55	1.56	1.06

Detector Material - NaI								
	0.1 MeV	0.5 MeV	1 MeV	2 MeV	4 MeV	6 MeV	8 MeV	10 MeV
1 cc	92.2	7.56	1.97	6.13E-1	1.80E-1	7.42E-2	4.08E-2	1.62E-2
2 cc	96.5	9.23	2.64	9.03E-1	2.73E-1	1.15E-1	5.61E-2	2.57E-2
5 cc	97.3	12.4	3.92	1.44	4.70E-1	2.01E-1	1.11E-1	5.31E-2
10 cc	98.1	15.6	5.29	2.05	7.16E-1	3.19E-1	1.82E-1	9.71E-2
20 cc	98.5	19.6	7.17	2.93	1.09	5.22E-1	2.99E-1	1.81E-1
50 cc	98.8	34.4	14.5	6.57	2.84	1.52	9.16E-1	5.88E-1
80 cc	95.5	39.8	18.0	8.57	3.84	2.19	1.40	9.42E-1

Table 3: Photon flux as a function of energy resolution centered about the Cl 6.11 MeV line.

Energy Resolution	100 ppm of TCA	Background
0.16%	3.48×10^{-7}	4.91×10^{-8}
1.0%	4.70×10^{-7}	1.78×10^{-7}
2.0%	7.96×10^{-7}	5.20×10^{-7}
3.0%	1.03×10^{-6}	7.68×10^{-7}

background at an energy resolution of 0.16% to being 1.3 times above background at an energy resolution of 3%. The Cd_9ZnTe_{10} has a measured energy resolution of about 2% at 1 MeV with increasing resolution at higher photon energies. This should be acceptable for detecting the 6.11 MeV line of Cl.

An optimal photon detector should have both high efficiency and energy resolution. Of the two commercially available detector materials, Ge and NaI, the Ge detectors are attractive because of their high energy resolution, However, they need to be operated around liquid-Nitrogen temperature. NaI detectors, in comparison, have higher efficiency but lower energy resolution. CdZnTe detectors, on the other hand, have energy resolution in between that of Ge and NaI detectors, but have the highest efficiency of the three, making it versatile for a wider range of applications. Furthermore, CdZnTe detectors could be operated at room temperature. We consider these properties ideal for this application. Modeling results henceforth assume a CdZnTe detector region. These results do not take into account the detector efficiency. The MCNP pulse height tally would have to be used in order to include this effect properly in the simulations. This pulse height tally is a true stochastic tally that does not allow variance reduction techniques such as cell or energy biasing. Using this tally would result in unacceptably long cpu times. However, rough estimates of detector efficiencies can be taken from this section.

The current MCNP interaction libraries do not include neutron interaction data for Zn or Te. The absorption cross sections for these elements are negligible compared to the absorption cross section of Cd. We therefore use a sphere of Cd to model the CdZnTe detector region. The data set for Cd neutron interactions used includes gamma-ray production.

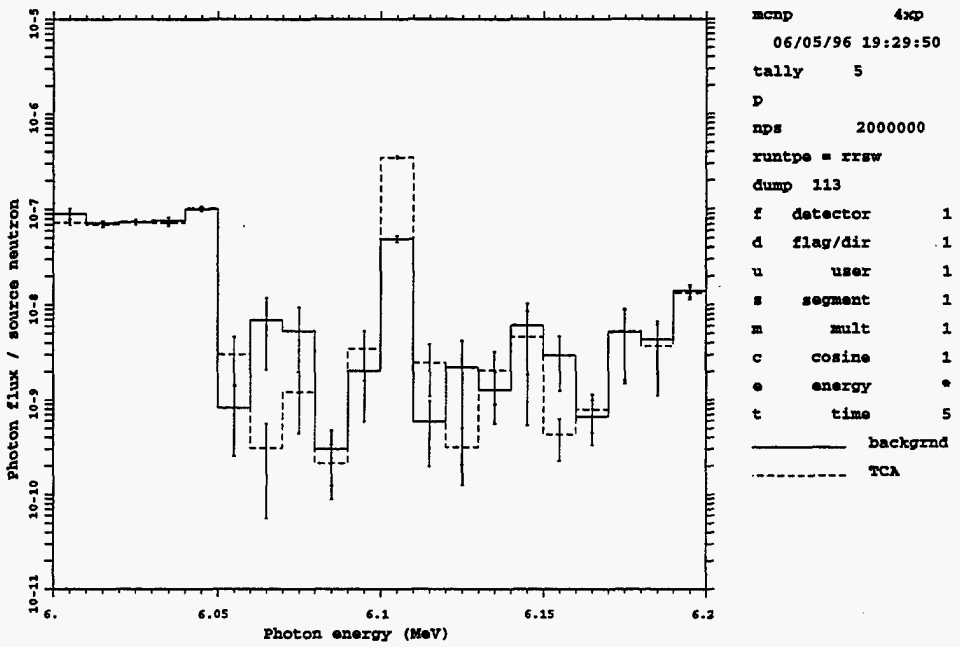

Figure 7: Photon flux versus photon energy for a wet sand medium (solid lines) and a uniform concentration at 100 ppm of TCA in wet sand (dash lines).

5 Results

Results are presented in this section. In all cases the photon fluxes are tallied after the first 30 μsec of the neutron pulse. The detector region is modeled as a Cd sphere for neutronics purposes. Photon flux is tallied at the center of the detector. The actual detector efficiency is not taken into account. Quantitative results are based on the 2.2 MeV photon line from thermal neutron capture in H for those cases containing only water. For cases containing TCA or salt water the 6.11 MeV line from thermal neutron capture in Cl is used.

5.1 Fractures in Granite and Uniform Concentrations in Wet Sand

A typical simulation geometry is depicted in Fig. 8 for detecting signals from fractures filled with water or TCA, where Region 4 is a 1-cm fracture volume between the $y = 10$ cm and $y = 11$ cm planes. Assumed densities are: water - 1.0 g/cc, granite - 2.50 g/cc, TCA-filled fracture - 1.0 g/cc TCA, and sand - 2.19 g/cc.

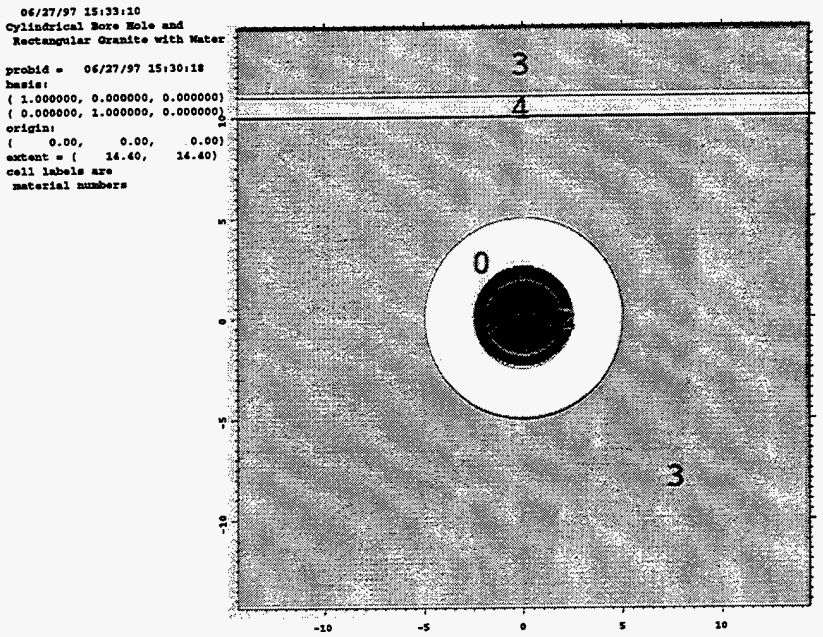

Figure 8: The $z = 0$ plane of a simulation geometry with a 1-cm x-z fracture at y = 10 cm: Region 0 is the cylindrical borehole, Region 1 the spherical Cd detector, Region 2 the B_4C neutron shield, Region 3 the medium and Region 4 the fracture.

Photon tallies of fracture cases are compared and analyzed with that of the base case containing no fracture. The model geometry is shown in Fig. 2. Fig. 9 shows the photon tally (photons/cm^2/source-neutron) of the base granite case (dashed line) versus that for the a 1-cm "incident" fracture of water, located between $y = 0$ *cm* and $y = 1$ *cm* planes (solid line). The 2.23 MeV peak is from thermal neutron capture in hydrogen (water).

The 2.23 MeV photon tallies (T's) and uncertainty ratios ($\triangle T/T$'s) for a 1-cm water fracture located at various distances d from the origin are listed in Table 4. Also listed in the table are quantities used to find the the range of detectability, defined as the maximum distance of the water fracture for which the 2.23 MeV tally is statistically higher than that of the base case. According to [6], a signal is detectable if $D \geq 2.33\sigma_b$, where

$$D = \frac{T - T_b}{T_b} \tag{1}$$

$$\sigma_b = \frac{1}{\sqrt{N_b}} \tag{2}$$

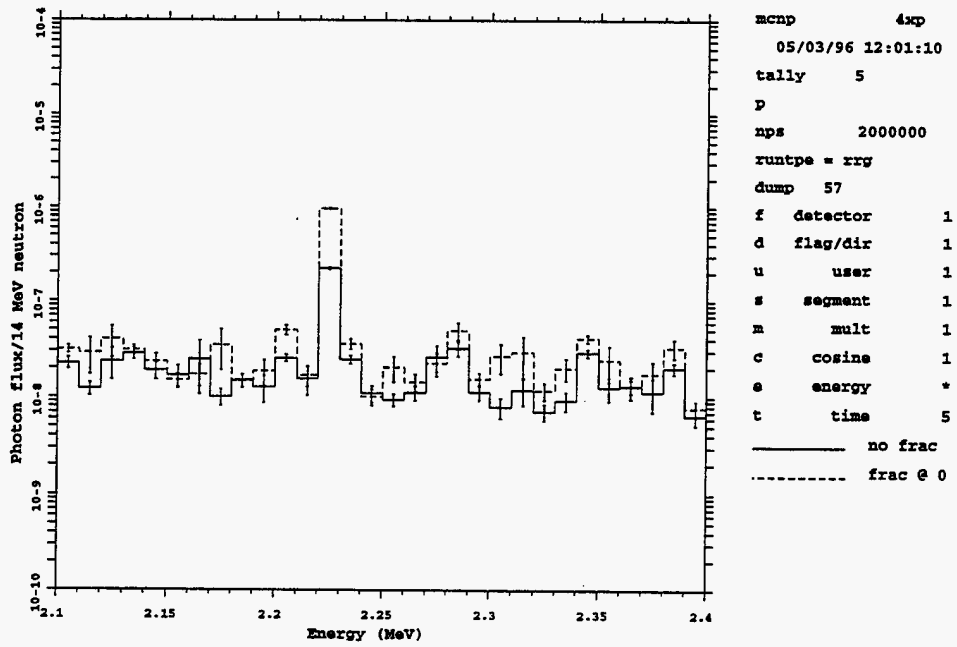

Figure 9: Photon tally (photons/cm^2/source-neutron) for granite medium, base case (solid curve) and photon tally for a 1-cm incident fracture of water in granite medium (dashed curve).

Table 4: Photon tally (γ/cm^2/source-neutron), tally uncertainty ratio, range and range uncertainty as a function of distance from a 1 cm water-filled fracture. Medium: granite. Neutrons: DT. Fracture: 1 cm; water.

$I = 10^7$ *n/sec* $(\sigma_b = 2.13 \times 10^{-2})$				
d (cm)	T (2.11 MeV)	$(\Delta T)/T$	$\mathcal{R}$	$\delta\mathcal{R}$
base	2.22×10^{-7}	0.0349	-	-
0	9.74×10^{-7}	0.0174	160	8.06
10	5.84×10^{-7}	0.0183	76.8	4.88
20	2.84×10^{-7}	0.0299	13.2	2.77

where T_b is the base tally, and N_b is the number of the base photon flux. For a neutron source of intensity I *(neutrons/sec)* running for t *sec*, then $N_b = I \times t \times T_b$. For example, a neutron source of intensity $I = 10^7$ (neutrons/sec) running for 10^3 sec leads to $N_b = 10^7 \times 10^3 \times (2.22 \times 10^{-7}) = 2.22 \times 10^3$ and $\sigma_b = 1/\sqrt{N_b} = 2.13 \times 10^{-2}$. In Table 4, $\mathcal{R}$ and $\delta\mathcal{R}$ are defined as,

$$\mathcal{R} = \frac{D}{\sigma_b} \tag{3}$$

$$\delta\mathcal{R} = \sqrt{\left[\frac{\triangle T}{T}\right]^2 + \left[\frac{\triangle T_b}{T_b}\right]^2}\ \frac{T}{T_b \sigma_b}\ . \tag{4}$$

Thus, if $\mathcal{R} > 2.33$, then the signal is detectable. $\delta\mathcal{R}$ is the uncertainty in $\mathcal{R}$. The functions

$$d = \alpha_R + \beta_R \log \mathcal{R} \tag{5}$$

$$d = \alpha_\delta + \beta_\delta \log(\delta\mathcal{R}) \tag{6}$$

are used to fit d to $\mathcal{R}$ and $\delta\mathcal{R}$. Using the data in Table 4, regression analysis gives

$$\begin{aligned} \alpha_R &= 40.30 \\ \beta_R &= -7.581 \\ \alpha_\delta &= 39.24 \\ \beta_\delta &= -18.70\ . \end{aligned}$$

The range, d_R, is found by extrapolating Eq. 5 to $\mathcal{R} = 2.33$. The uncertainty in the range, $\triangle d_R$, is obtained also by extrapolating to the range d_R (at which $\mathcal{R} = 2.33$). Substituting α_R and β_R into Eq. (5), with $\mathcal{R} = 2.33$ gives $d_R = 34\ cm$. Using both Eqs. (5) and (6), the uncertainty in the range $\triangle d_R$ is

$$\delta R = \exp\left[\frac{d_R - \alpha_\delta}{\beta_\delta}\right] = 1.323 \tag{7}$$

$$\triangle d_R = \left|\beta_R \frac{(\delta R)}{\mathcal{R}}\right| = 4\ cm \tag{8}$$

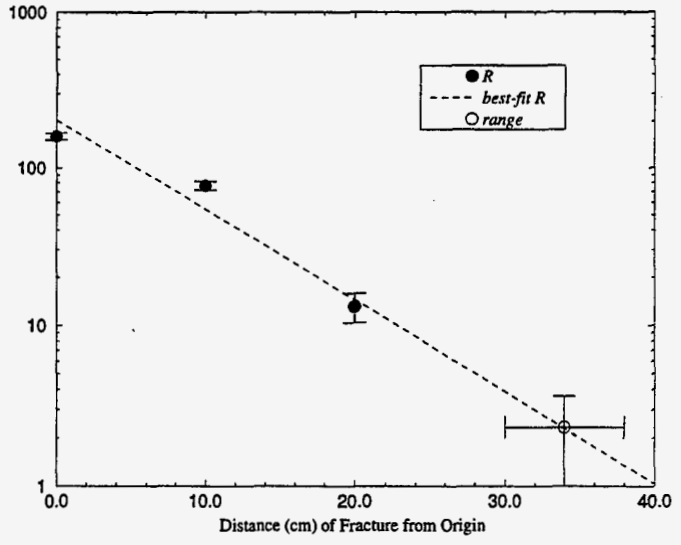

Figure 10: $\mathcal{R}$ (black circles), the best-fit function (dashed line) versus d, and the extrapolated range d_R (open circle).

Fig. 10 shows the three data points of $\mathcal{R}$, the best-fit function $d = \alpha_R + \beta_R \log R$ versus d, and the range d_R.

The above results are derived assuming a neutron source intensity $I = 10^7$ *(neutrons/sec)*, leading to $\sigma_b = 2.132 \times 10^{-2}$. The ranges and their uncertainties are similarly calculated for source intensities $I = 10^8$ *(neutrons/sec)* ($\sigma_b = 6.742 \times 10^{-3}$) in Table 5. Note that $\mathcal{R}$ and $\delta\mathcal{R}$ are larger than those in Table 4 by a factor of $\sqrt{10}$ since σ_b is smaller (by a factor of $\sqrt{10}$) for a higher intensity (by a factor of 10). Here $\mathcal{R}$ and $\delta\mathcal{R}$ are fitted with

$$d = 49.03 - 7.581 \log \mathcal{R} \tag{9}$$

$$d = 60.77 - 18.70 \log(\delta\mathcal{R}) \ , \tag{10}$$

leading to $d_R = 43\ cm$ and an uncertainty $\triangle d_R = 9\ cm$.

Lastly, for $I = 10^9$ *(neutrons/sec)* ($\sigma_b = 2.132 \times 10^{-3}$), the statistical quantities are listed in Table 6, with $\mathcal{R}$ and $\delta\mathcal{R}$ a factor of $\sqrt{100}$ larger than those in Table 4 since σ_b is smaller (by a factor of $\sqrt{100}$) for a higher intensity (by a factor of 100). Also $\mathcal{R}$ and $\delta\mathcal{R}$ here are

Table 5: Range and uncertainty for a 1 cm water-filled fracture in a granite media. DT neutrons are assumed as the source at an intensity of 10^8 n/sec.

$I = 10^8$ *n/sec* $(\sigma_b = 6.71 \times 10^{-3})$		
d (cm)	$\mathcal{R}$	δR
base	-	-
0	505	25.5
10	243	15.4
20	41.6	8.76

Table 6: Range and uncertainty for a 1 cm water-filled fracture in a granite media. DT neutrons are assumed as the source at an intensity of 10^9 n/sec.

$I = 10^9$ *n/sec* $(\sigma_b = 2.12 \times 10^{-3})$		
d (cm)	$\mathcal{R}$	δR
base	-	-
0	1600	80.6
10	768	48.8
20	132	27.7

fitted with

$$d = 57.76 - 7.581 \log \mathcal{R} \quad (11)$$

$$d = 82.30 - 18.70 \log(\delta \mathcal{R}) \ , \quad (12)$$

leading to $d_R = 51\ cm$ and an uncertainty $\triangle d_R = 17\ cm$.

The ranges and the associated uncertainties for 1-cm water-filled fracture in granites are summarized in Table 8. Results from MCNP runs and data analysis for other cases, similar to those listed in Table 4, are listed in tables in the Appendix. The following is a list of tables of range versus intensity of the neutron source, similar to Table 8. *It is important to note that curve fitting of the few (three or less) data points and then extrapolating to the*

Table 7: Index of Tables containing the results.

Table #	Medium	Neutrons	Fracture Size (cm)	Material in Fracture
8	granite	DT	1.0	water
9	wet granite	DT	1.0	water
10	granite	DT	1.0	salt water
11	granite	DT	0.1	salt water
12	wet granite	DT	1.0	salt water
13	wet granite	DT	0.1	salt water
14	granite	DT	1.0	TCA (1 g/cc)
15	granite	DT	0.1	TCA (1 g/cc)
16	granite	DT	0.1	TCA (0.1 g/cc)
17	wet granite	DT	1	TCA (0.1 g/cc)
18	granite	DD	0.1	TCA (1 g/cc)
19	granite	DT	1 @ 0 cm	TCA
20	granite	DT	1 @ 15 cm	TCA
21	wet sand	DT	-	TCA (ppm)
22	wet sand	DT	-	Pb (ppm)

range will yield results that are quite sensitive to the fitting functions. Most of the data are fitted with $\mathcal{R} \sim e^{-d}$ *and* $\delta\mathcal{R} \sim e^{d}$. The cases of 0.1-cm fractures of water in granite, wet or dry, are not included due to lack of signal. Water has density 1 g/cc; wet granite has uniform density of 0.3 g/cc water; salt water has density 1.3 g/cc which includes 0.3 g/cc of NaCl. In tables 8 to 18, the range is defined as the maximum distance of a fracture with a detectable signal. In tables 19 and 20, the range is defined as the minimum density in a fracture with a detectable signal (fracture is located at a fixed distance). In Tables 21 and 22, the range is defined as the minimum uniform concentration in a medium with a detectable signal.

Table 8: Medium: granite. Neutrons: DT. Fracture: 1 cm; water.

2.23 MeV signal			
Intensity (n/sec)	10^7	10^8	10^9
d_R (cm)	34	43	51
$\triangle d_R$ (cm)	4	9	17

Table 9: Medium: wet granite. Neutrons: DT. Fracture: 1 cm; water.

2.23 MeV signal			
Intensity (n/sec)	10^7	10^8	10^9
d_R (cm)	21	27	34
$\triangle d_R$ (cm)	2	4	6

Table 10: Medium: granite. Neutrons: DT. Fracture: 1 cm; salt water.

6.11 MeV signal			
Intensity (n/sec)	10^7	10^8	10^9
d_R (cm)	42	51	60
$\triangle d_R$ (cm)	4	7	11

Table 11: Medium: granite. Neutrons: DT. Fracture: 0.1 cm; salt water.

6.11 MeV signal			
Intensity (n/sec)	10^7	10^8	10^9
d_R (cm)	30	42	54
$\triangle d_R$ (cm)	4	8	15

Table 12: Medium: wet granite. Neutrons: DT. Fracture: 1 cm; salt water.

6.11 MeV signal			
Intensity (n/sec)	10^7	10^8	10^9
d_R (cm)	45	55	65
$\triangle d_R$ (cm)	5	8	14

Table 13: Medium: wet granite. Neutrons: DT. Fracture: 0.1 cm; salt water.

6.11 MeV signal			
Intensity (n/sec)	10^7	10^8	10^9
d_R (cm)	28	38	48
$\triangle d_R$ (cm)	4	8	16

Table 14: Medium: granite. Neutrons: DT. Fracture: 1 cm; TCA (1 g/cc).

6.11 MeV signal			
Intensity (n/sec)	10^7	10^8	10^9
d_R (cm)	47	57	66
$\triangle d_R$ (cm)	4	6	8

Table 15: Medium: granite. Neutrons: DT. Fracture: 0.1 cm; TCA (1 g/cc).

6.11 MeV signal			
Intensity (n/sec)	10^7	10^8	10^9
d_R (cm)	40	51	62
$\triangle d_R$ (cm)	3	5	7

Table 16: Medium: granite. Neutrons: DT. Fracture: 0.1 cm; TCA (0.1 g/cc).

6.11 MeV signal			
Intensity (n/sec)	10^7	10^8	10^9
d_R (cm)	36	45	54
$\triangle d_R$ (cm)	3	4	6

Table 17: Medium: wet granite. Neutrons: DT. Fracture: 1 cm; TCA (1 g/cc).

6.11 MeV signal			
Intensity (n/sec)	10^7	10^8	10^9
d_R (cm)	47	56	65
$\triangle d_R$ (cm)	3	5	8

Table 18: Medium: granite. Neutrons: DD. Fracture: 0.1 cm; TCA (1 g/cc).

6.11 MeV signal			
Intensity (n/sec)	10^7	10^8	10^9
d_R (cm)	54	64	74
$\triangle d_R$ (cm)	3	3	4

Table 19: Medium: granite. Neutrons: DT. Fracture: 0.1 cm; TCA. Location: 0 cm.

6.11 MeV signal			
Intensity (n/sec)	10^7	10^8	10^9
densities (g/cc)	7.4×10^{-3}	2.0×10^{-3}	5.3×10^{-4}
uncertainty (g/cc)	1.8×10^{-3}	6.4×10^{-4}	2.3×10^{-4}

Table 20: Medium: granite. Neutrons: DT. Fracture: 0.1 cm; TCA. Location: 15 cm.

6.11 MeV signal			
Intensity (n/sec)	10^7	10^8	10^9
densities (g/cc)	4.8×10^{-2}	1.4×10^{-2}	4.0×10^{-3}
uncertainty (g/cc)	1.3×10^{-2}	5.7×10^{-3}	2.5×10^{-3}

Table 21: Medium: wet sand. Neutrons: DT. Material in Medium: TCA (ppm).

6.11 MeV signal			
Intensity (n/sec)	10^7	10^8	10^9
concentrations (ppm)	2.00	0.83	0.50
uncertainty (ppm)	0.71	0.38	0.26

Table 22: Medium: wet sand. Neutrons: DT. Material in Medium: Pb (ppm).

7.38 MeV signal			
Intensity (n/sec)	10^7	10^8	10^9
concentrations (ppm)	230	120	20
uncertainty (ppm)	230	120	20

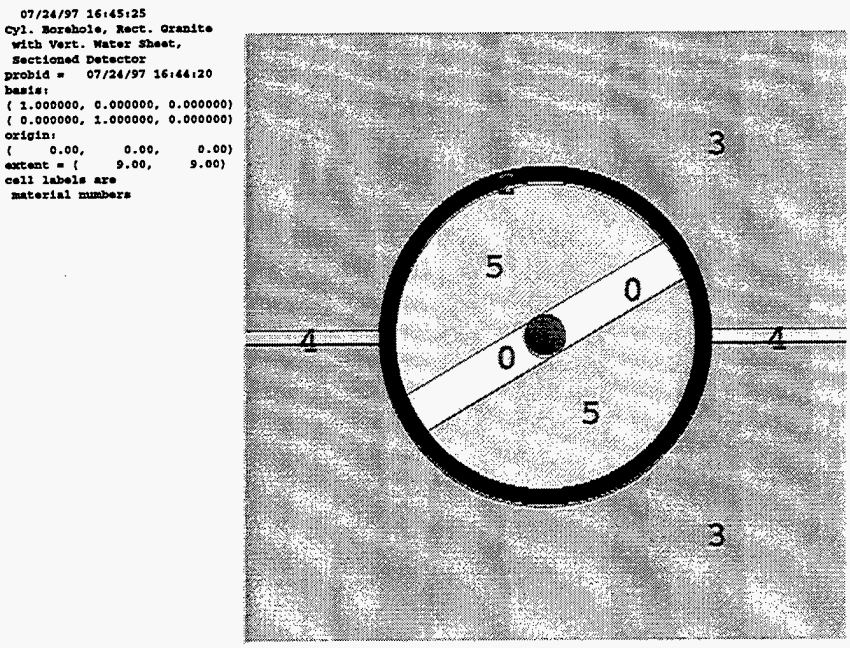

Figure 11: The $z = 0$ plane of a simulation geometry: Region 0 is the gap, Region 1 the spherical 1 cm^3 Cd detector, Region 2 the B_4C neutron shield, Region 3 the granite medium, Region 4 the 0.1-cm fracture (exaggerated in size) of salt water (with $\rho = 0.3\ g/cc$ NaCl) and Region 5 the W photon shield ($\rho = 19.3\ g/cc$).

5.2 Angular Dependence of Incident Fractures

The MCNP geometry for a case with an incident fracture is depicted in Fig. 11 (magnified view of the $z = 0$ plane). Region 4 is a 1-mm fracture of salt water (0.3 g/cc NaCl in water). ($\rho = 19.3\ g/cc$). Region 0 is a parallel-plane gap, 0.6-cm thick and at 30 degrees with respect to the fracture, in the photon shield.[2] Results of photon tallies for the gap rotated from 0 to 90 degrees are shown in Figs. 12 and 13. In Fig. 13, the normalized tallies are plotted to compare the relative width of the maxima. The maxima occurs when the gap is at 0-degree with respect to the fracture. The maximum of the Cl signal is about an order of magnitude higher than its neighbor, whereas the maximum of the H signal is about twice as high as its neighbor [7].

[2]Results were also obtained for a 1.2-cm thick gap in the W shield. The smaller gap thickness produces a sharper (narrower) peak, hence localizing the incident fracture better. However a very small gap thickness would let in too few incoming photons, and could result in statistically unreliable data.

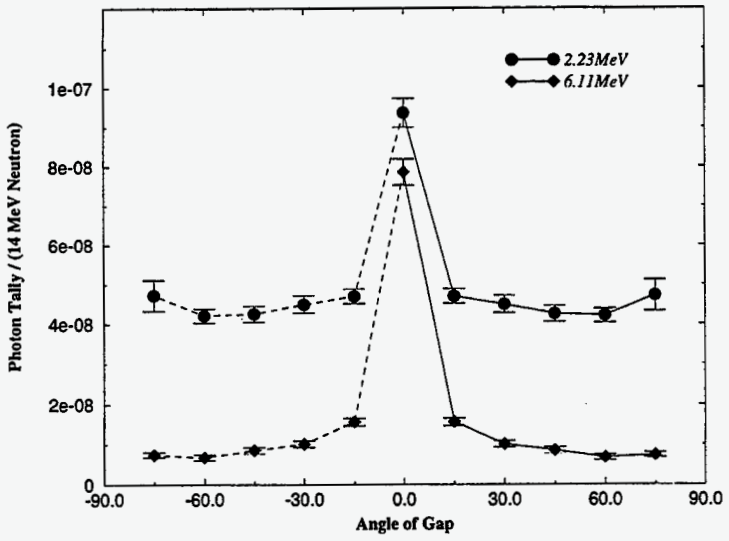

Figure 12: Photon tallies at 2.23 and 6.11 MeV for a 1-mm salt water fracture versus angle of the photon gap.

6 Conclusions

From our geometrical setups (see Fig. 8), MCNP results and data analysis show that it is possible to detect signal of the 2.33 MeV photon line of H in granite for a 1-cm fracture of water located out to 34 ± 4 *cm* with a neutron source intensity of 10^7 *DT neutron/sec* running for 10^3 sec (Table 8).

However, it is not possible to detect any signal for 0.1-cm fractures beyond the neighborhood of the origin. Furthermore, if the granite medium is saturated with a uniform density of 0.1 g/cc water, all the ranges of the H line diminish significantly (see Table 9).

In comparison, the 6.11 MeV Cl signal from only a 0.3 g/cc density of NaCl in fractures of water has longer ranges than those of H (Tables 10 and 11). In fact, the range of the Cl signal for granite saturated with water (Tables 12 and 13) are slightly higher than those for dry granite, due to the good moderating effect of H in water. Fig. 14 illustrates the superior properties of the Cl signal relative to the H signal. However, the Cl signal cannot be used in naturally saline environments.

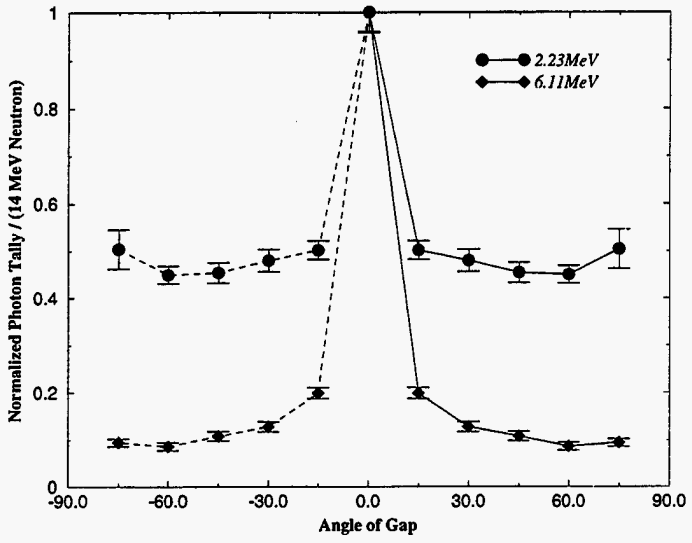

Figure 13: Normalized photon tallies at 2.23 and 6.11 MeV for a 1-mm salt water fracture versus angle of the photon gap.

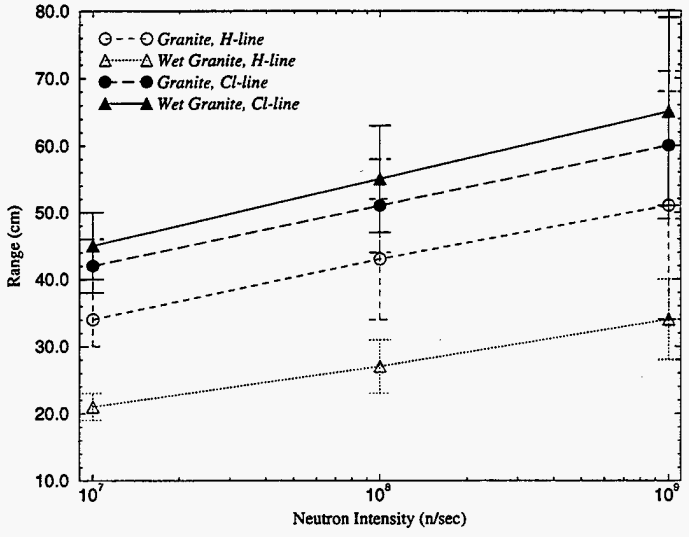

Figure 14: Range versus neutron intensity of H (2.33 MeV) and Cl (6.11 MeV) lines for 1-cm and 0.1-cm fractures of water and salt water.

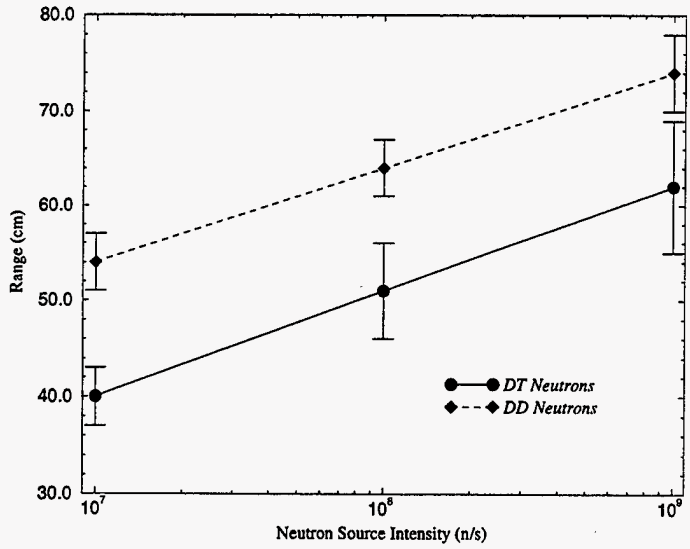

Figure 15: Range versus DT and DD Neutron Intensity for a 0.1-cm fracture of TCA (1 g/cc) in granite.

Results and analyses also show that the Cl signal from TCA-filled fractures (Tables 14 to 17), are detectable to even longer ranges than fractures of salt water (Tables 10 to 13), due to the higher concentration of Cl in TCA than in salt water. Similarly, the range of the Cl signal from TCA increases slightly for granite saturated with water.

Fig. 15 compares the ranges from using DT and DD neutrons for the case of a 0.1-cm fracture of TCA. DD neutrons, as discussed before, give longer ranges and smaller errors.

The Cl signal from lower densities of TCA in 0.1-cm fractures can be detected, from $\sim 10^{-2}$ to 10^{-3} g/cc, depending on location and neutron intensity (Tables 19 and 20).

Also detectable is the Cl signal for small uniform concentration of TCA, about $10^{-1} ppm$ (21), in wet sand. Detection of uniform concentrations of Pb is more difficult. We use the 7.38 MeV line for detection [2]. As can be seen in Table 22 much higher concentrations are required for detection as compared to Cl. The error bar is quite high due to the relatively low photon production at 7.38 MeV. Detectable Pb concentrations vary from about 200 ppm for a neutron source intensity of 10^7 n/sec to 20 ppm for 10^9 n/sec.

Lastly, Figs. 12 and 13 suggest that it is possible to detect the angular location of an

incident 1mm fracture of salt water by its Cl signal, where the coincident signal (photon-shield gap lining up with fracture) is about ten times that of non-coincident signals. Future work may realize gains from an optimization of detector shielding and collimator geometry.

References

[1] *MCNP - A General Monte Carlo N-Particle Transport Code, Version 4B*, J. F. Briesmeister, Ed., Los Alamos National Lab, 1997.

[2] Stephanie C. Frankle, *Photon Production Assessment for the MCNP Data Libraries*, Los Alamos Publications, **LA-13092-MS**, (1996).

[3] R. A. Forster, R. C. Little, J. F. Briesmeister and J. S. Hendricks, *MCNP Capabilities For Nuclear Well Logging Calculations*, IEEE Transactions on Nuclear Science, **37**, 1378-1384 (1990).

[4] *Handbook on Nuclear Data for Borehole Logging and Mineral Analysis*, Technical Report Series No. 357, International Atomic Energy Agency, Vienna, 1993.

[5] E. Greenspan, W. G. Price and H. Fishman, *SWAN - A Code for the Analysis and Optimization of Fusion Reactor Nucleonic Characteristics,* Princeton Plasma Physics Laboratory Report MATT-1008 (1973).

[6] Loyld A. Currie, *Limits of Qualitative Detection and Quantitative Determination*, Analytical Chemistry, **40**, 586-593 (1968).

[7] C. M. Celata, M. Amman, R. Donahue, K. N. Leung, P. N. Luke, L. T. Perkins, P. T. Zawislanski and D. Hua, *A New Intense Neutron Tool for Radiography and Detection of Water and Ground Contaminants,* presented during the **1997 IEEE Particle Accelerator Conference** in Vancouver, BC, Canada, May 1997.

A Appendix

A.1 Tables of MCNP Data

Tables for MCNP tallies T, uncertainty ratios $\Delta T/T$, statistical quantities $\mathcal{R}$ and $\delta\mathcal{R}$ are listed, all assuming a neutron source intensity of 10^7 *neutrons/sec* running for 10^3 *secs* (hence, $\sigma_b = 1/\sqrt{10^{10}T_b}$). Water has density 1 g/cc; wet granite has uniform density of 0.3 g/cc water; salt water has density 1.3 g/cc which includes 0.3 g/cc of NaCl. The following is a list of the tables.

Table	Medium	Neutrons	Fracture Size (cm)	Material in Fracture
4	granite	DT	1.0	water
23	wet granite	DT	1.0	water
24	granite	DT	1.0	salt water
25	granite	DT	0.1	salt water
26	wet granite	DT	1.0	salt water
27	wet granite	DT	0.1	salt water
28	granite	DT	1.0	TCA (1 g/cc)
29	granite	DT	0.1	TCA (1 g/cc)
30	granite	DT	0.1	TCA (0.1 g/cc)
31	wet granite	DT	1	TCA (0.1 g/cc)
32	granite	DD	0.1	TCA (1 g/cc)
33	granite	DT	1 @ 0 cm	TCA
34	granite	DT	1 @ 15 cm	TCA
35	wet sand	DT	-	TCA (ppm)
36	wet sand	DT	-	Pb (ppm)

Table 23: Medium: wet granite. Neutrons: DT. Fracture: 1 cm; water.

$I = 10^7$ *n/sec* $(\sigma_b = 6.47 \times 10^{-3})$				
d (cm)	T (2.23 MeV)	$(\triangle T)/T$	$\mathcal{R}$	δR
base	2.39×10^{-6}	0.0111	-	-
0	3.53×10^{-6}	0.0094	73.7	3.32
10	2.98×10^{-6}	0.0265	38.2	5.54
20	2.43×10^{-6}	0.0106	2.59	2.41

Table 24: Medium: granite. Neutrons: DT. Fracture: 1 cm; salt water.

$I = 10^7$ *n/sec* $(\sigma_b = 7.09 \times 10^{-2})$				
d (cm)	T (6.11 MeV)	$(\triangle T)/T$	$\mathcal{R}$	δR
base	1.99×10^{-8}	0.0607	-	-
0	6.59×10^{-7}	0.0216	453	30.1
20	1.08×10^{-7}	0.0356	62.5	5.39
40	2.36×10^{-8}	0.0747	2.62	1.61

Table 25: Medium: granite. Neutrons: DT. Fracture: 0.1 cm; salt water.

$I = 10^7$ *n/sec* $(\sigma_b = 7.09 \times 10^{-2})$				
d (cm)	T (6.11 MeV)	$(\triangle T)/T$	$\mathcal{R}$	δR
base	1.99×10^{-8}	0.0607	-	-
0	7.24×10^{-8}	0.0284	37.2	3.44
20	2.80×10^{-8}	0.0417	5.74	1.46

Table 26: Medium: wet granite. Neutrons: DT. Fracture: 1 cm; salt water.

$I = 10^7$ *n/sec* $(\sigma_b = 4.84 \times 10^{-2})$				
d (cm)	T (6.11 MeV)	$(\Delta T)/T$	$\mathcal{R}$	δR
base	4.27×10^{-8}	0.0404	-	-
0	9.87×10^{-7}	0.0180	457	21.1
20	1.51×10^{-7}	0.0499	52.4	4.69
40	5.10×10^{-8}	0.0711	4.01	2.02

Table 27: Medium: wet granite. Neutrons: DT. Fracture: 0.1 cm; salt water.

$I = 10^7$ *n/sec* $(\sigma_b = 4.84 \times 10^{-2})$				
d (cm)	T (6.11 MeV)	$(\Delta T)/T$	$\mathcal{R}$	δR
base	4.27×10^{-8}	0.0404	-	-
0	1.65×10^{-7}	0.0245	59.2	3.77
20	5.51×10^{-8}	0.0408	6.00	1.53

Table 28: Medium: granite. Neutrons: DT. Fracture: 1 cm; TCA (1 g/cc).

$I = 10^7$ *n/sec* $(\sigma_b = 7.09 \times 10^{-2})$				
d (cm)	T (6.11 MeV)	$(\Delta T)/T$	$\mathcal{R}$	δR
base	1.99×10^{-8}	0.0607	-	-
0	1.11×10^{-6}	0.0092	773	48.3
20	1.48×10^{-7}	0.0141	90.8	6.54
40	3.02×10^{-8}	0.0399	7.30	1.56

Table 29: Medium: granite. Neutrons: DT. Fracture: 0.1 cm; TCA (1 g/cc).

$I = 10^7$ *n/sec* $(\sigma_b = 7.09 \times 10^{-2})$				
d (cm)	T (6.11 MeV)	$(\triangle T)/T$	$\mathcal{R}$	δR
base	1.99×10^{-8}	0.0607	-	-
0	2.39×10^{-7}	0.0170	155	10.7
10	1.31×10^{-7}	0.0165	78.8	5.84
20	4.95×10^{-8}	0.0285	21.0	2.35
30	2.97×10^{-8}	0.0525	6.95	1.69

Table 30: Medium: granite. Neutrons: DT. Fracture: 0.1 cm; TCA (0.1 g/cc).

$I = 10^7$ *n/sec* $(\sigma_b = 7.09 \times 10^{-2})$				
d (cm)	T (6.11 MeV)	$(\triangle T)/T$	$\mathcal{R}$	δR
base	1.99×10^{-8}	0.0607	-	-
0	3.10×10^{-7}	0.0148	206	13.7
10	1.31×10^{-7}	0.0171	78.8	5.86
20	4.80×10^{-8}	0.0281	19.9	2.28
30	2.67×10^{-8}	0.0448	4.82	1.43

Table 31: Medium: wet granite. Neutrons: DT. Fracture: 1 cm; TCA (1 g/cc).

$I = 10^7$ *n/sec* $(\sigma_b = 4.84 \times 10^{-2})$				
d (cm)	T (6.11 MeV)	$(\triangle T)/T$	$\mathcal{R}$	δR
base	4.27×10^{-8}	0.0404	-	-
0	1.97×10^{-6}	0.0135	933	40.6
20	2.30×10^{-7}	0.0341	90.6	5.88
40	5.42×10^{-8}	0.0660	5.57	2.03

Table 32: Medium: granite. Neutrons: DD. Fracture: 1 cm; TCA (1 g/cc).

$I = 10^7$ *n/sec* $(\sigma_b = 5.60 \times 10^{-2})$				
d (cm)	T (6.11 MeV)	$(\triangle T)/T$	$\mathcal{R}$	δR
base	3.19×10^{-8}	0.0728	-	-
0	2.00×10^{-6}	0.0134	1100	82.9
20	2.53×10^{-7}	0.0155	124	10.5
40	5.17×10^{-8}	0.0554	11.1	2.64

Table 33: Medium: granite. Neutrons: DT. Fracture: 0.1 cm; TCA. Location: 0 cm.

$I = 10^7$ *n/sec* $(\sigma_b = 7.09 \times 10^{-2})$				
Density (g/cc)	T (6.11 MeV)	$(\triangle T)/T$	$\mathcal{R}$	δR
base	1.99×10^{-8}	0.0607	-	-
1.0	2.39×10^{-7}	0.0170	155	10.6
0.5	1.62×10^{-7}	0.0280	101	7.68
0.1	5.10×10^{-8}	0.0340	22.0	2.52

Table 34: Medium: granite. Neutrons: DT. Fracture: 0.1 cm; TCA. Location: 15 cm.

$I = 10^7$ *n/sec* $(\sigma_b = 7.09 \times 10^{-2})$				
Density (g/cc)	T (6.11 MeV)	$(\triangle T)/T$	$\mathcal{R}$	δR
base	1.99×10^{-8}	0.0607	-	-
1.0	7.58×10^{-8}	0.0201	39.6	3.44
0.75	6.38×10^{-8}	0.0208	31.1	2.90
0.50	4.93×10^{-8}	0.0245	20.8	2.29

Table 35: Medium: wet sand. Neutrons: DT. Material: TCA (ppm).

$I = 10^7$ *n/sec* $(\sigma_b = 4.51 \times 10^{-2})$				
Concentration (ppm)	T (6.11 MeV)	$(\Delta T)/T$	$\mathcal{R}$	δR
base	4.91×10^{-8}	0.0733	-	-
1000	2.39×10^{-6}	0.0108	1060	79.9
100	3.48×10^{-7}	0.0282	135	12.3
10	7.93×10^{-8}	0.0585	13.6	3.36

Table 36: Medium: wet sand. Neutrons: DT. Material: Pb (ppm).

$I = 10^7$ *n/sec* $(\sigma_b = 4.51 \times 10^{-2})$				
Concentration (ppm)	T (6.11 MeV)	$(\Delta T)/T$	$\mathcal{R}$	δR
base	4.01×10^{-10}	0.92	-	-
10^5	2.76×10^{-7}	0.02	1380	1270
10^3	3.13×10^{-9}	0.26	13.6	14.9
10^2	4.94×10^{-10}	0.48	0.464	2.56

A.2 A Sample MCNP Code

Below is a MCNP code simulating the release of 8×10^6 14-MeV neutrons in a granite medium with a 1-cm thick fracture of salt water (0.3 g/cc NaCl) located at 20 cm away from the detector.

```
Cyl. Bore Hole and Rectangular Granite with a 1cm-thick Fracture of Salt Water
C     Cell Cards are made up of five sets of numbers:
C       (1) Cell number, (2) Material Card number, (3) Mass Densities,
C       (4) Boundary Surfaces, (5) Cell biasing factors
C
C     Cd Detector with B_4C Shield
11    1  -2.58   -10                                  imp:n=4.4E-3 imp:p=5.8E-3
21    2  -2.255  -20   10                            imp:n=3.6E-3 imp:p=1.6E-3
C
C     Borehole Geometry: cylindrical slabs
31    0           20   510 -610 -30                  imp:n=3.6E-3 imp:p=1.6E-3
41    0         (-510  520 -30):(610 -620 -30)       imp:n=3.3E-3 imp:p=4.0E-4
51    0         (-520  530 -30):(620 -630 -30)       imp:n=2.6E-3 imp:p=1.8E-4
61    0         (-530  540 -30):(630 -640 -30)       imp:n=1.6E-3 imp:p=5.8E-5
71    0         (-540  550 -30):(640 -650 -30)       imp:n=7.4E-4 imp:p=1.7E-5
81    0         (-550  560 -30):(650 -660 -30)       imp:n=2.5E-4 imp:p=4.5E-6
91    0         (-560  570 -30):(660 -670 -30)       imp:n=6.6E-5 imp:p=1.2E-6
101   0         (-570  580 -30):(670 -680 -30)       imp:n=1.4E-5 imp:p=3.4E-7
C
C     Granite Geometry: nested cubic boxes
C       Cells with 500's numbers are granite, 800's are salt water.
C
C       First Cubic Box
511   3  -2.50   120 -220  320 -420  520 -620 30
                                                    imp:n=3.3E-3 imp:p=4.0E-4
C       Second Cubic Box
521   3  -2.50 (30 130 -230 330 -430 -520 530):(30 130 -230 330 -430 620 -630)
             :(130 -230 330 -320 520 -620):(130 -230 420 -430 520 -620)
             :(130 -120 320 -420 520 -620):(220 -230 320 -420 520 -620)
                                                    imp:n=2.6E-3 imp:p=1.8E-4
C       Third Cubic Box
831   4  -1.30   140 -240  810 -820  540 -640
```

```
                                                    imp:n=1.6E-3 imp:p=5.8E-5
531   3  -2.50 (30 140 -240 340 -810 -530 540):(30 140 -240 820 -440 -530 540)
           :(30 140 -240 340 -810 630 -640):(30 140 -240 820 -440 630 -640)
           :(140 -240 340 -330 530 -630):(140 -240 430 -810 530 -630)
           :(140 -240 820 -440 530 -630)
           :(140 -130 330 -430 530 -630):(230 -240 330 -430 530 -630)
                                                    imp:n=1.6E-3 imp:p=5.8E-5
C        Fourth Cubic Box
841   4  -1.30 (30 150 -250 810 -820 -540 550):(30 150 -250 810 -820 640 -650)
           :(150 -140 810 -820 540 -640):(240 -250 810 -820 540 -640)
                                                    imp:n=7.4E-4 imp:p=1.7E-5
541   3  -2.50 (30 150 -250 350 -810 -540 550):(30 150 -250 820 -450 -540 550)
           :(30 150 -250 350 -810 640 -650):(30 150 -250 820 -450 640 -650)
           :(150 -250 350 -340 540 -640):(150 -250 440 -450 540 -640)
           :(150 -140 340 -810 540 -640):(150 -140 820 -440 540 -640)
           :(240 -250 340 -810 540 -640):(240 -250 820 -440 540 -640)
                                                    imp:n=7.4E-4 imp:p=1.7E-5
C        Fifth Cubic Box
851   4  -1.30 (30 160 -260 810 -820 -550 560):(30 160 -260 810 -820 650 -660)
           :(160 -150 810 -820 550 -650):(250 -260 810 -820 550 -650)
                                                    imp:n=2.5E-4 imp:p=4.5E-6
551   3  -2.50 (30 160 -260 360 -810 -550 560):(30 160 -260 820 -460 -550 560)
           :(30 160 -260 360 -810 650 -660):(30 160 -260 820 -460 650 -660)
           :(160 -260 360 -350 550 -650):(160 -260 450 -460 550 -650)
           :(160 -150 350 -810 550 -650):(160 -150 820 -450 550 -650)
           :(250 -260 350 -810 550 -650):(250 -260 820 -450 550 -650)
                                                    imp:n=2.5E-4 imp:p=4.5E-6
C        Sixth Cubic Box
861   4  -1.30 (30 170 -270 810 -820 -560 570):(30 170 -270 810 -820 660 -670)
           :(170 -160 810 -820 560 -660):(260 -270 810 -820 560 -660)
                                                    imp:n=6.6E-5 imp:p=1.2E-6
561   3  -2.50 (30 170 -270 370 -810 -560 570):(30 170 -270 820 -470 -560 570)
           :(30 170 -270 370 -810 660 -670):(30 170 -270 820 -470 660 -670)
           :(170 -270 370 -360 560 -660):(170 -270 460 -470 560 -660)
           :(170 -160 360 -810 560 -660):(170 -160 820 -460 560 -660)
           :(260 -270 360 -810 560 -660):(260 -270 820 -460 560 -660)
                                                    imp:n=6.6E-5 imp:p=1.2E-6
C        Seventh Cubic Box
871   4  -1.30 (30 180 -280 810 -820 -570 580):(30 180 -280 810 -820 670 -680)
           :(180 -170 810 -820 570 -670):(270 -280 810 -820 570 -670)
```

```
                                                    imp:n=1.4E-5 imp:p=3.4E-7
571   3  -2.50 (30 180 -280 380 -810 -570 580):(30 180 -280 820 -480 -570 580)
                :(30 180 -280 380 -810 670 -680):(30 180 -280 820 -480 670 -680)
                :(180 -280 380 -370 570 -670):(180 -280 470 -480 570 -670)
                :(180 -170 370 -810 570 -670):(180 -170 820 -470 570 -670)
                :(270 -280 370 -810 570 -670):(270 -280 820 -470 570 -670)
                                                    imp:n=1.4E-5 imp:p=3.4E-7
C         Outside Void
9999  0          -180:280:-380:480:-580:680        imp:n=0 imp:p=0

C
C
C     Surface Cards have 3 sets of inputs:
C        (1) surface number, (2) surface character (plane, sphere etc) and
C        (3) location of surface
10         so     2      $Cd Sphere
20         so     2.5    $B4C Shield
30         cz     5      $cylinder of radius 5 cm,  center at origin
C     yz-planes
120        px    -9.584     $yz-plane
220        px     9.584     $yz-plane
130        px    -18.296    $yz-plane
230        px     18.296    $yz-plane
140        px    -29.622    $yz-plane
240        px     29.622    $yz-plane
150        px    -43.562    $yz-plane
250        px     43.562    $yz-plane
160        px    -59.244    $yz-plane
260        px     59.244    $yz-plane
170        px    -74.926    $yz-plane
270        px     74.926    $yz-plane
180        px    -87.123    $yz-plane
280        px     87.123    $yz-plane
C     xz-Surfaces
320        py    -9.584     $xz-plane
420        py     9.584     $xz-plane
330        py    -18.296    $xz-plane
430        py     18.296    $xz-plane
340        py    -29.622    $xz-plane
440        py     29.622    $xz-plane
```

```
350       py    -43.562    $xz-plane
450       py     43.562    $xz-plane
360       py    -59.244    $xz-plane
460       py     59.244    $xz-plane
370       py    -74.926    $xz-plane
470       py     74.926    $xz-plane
380       py    -87.123    $xz-plane
480       py     87.123    $xz-plane
810       py     20.0      $xz-plane
820       py     21.0      $xz-plane
C     xy-Surfaces
510       pz    -4.356     $xy-plane
610       pz     4.356     $xy-plane
520       pz    -9.584     $xy-plane
620       pz     9.584     $xy-plane
530       pz    -18.296    $xy-plane
630       pz     18.296    $xy-plane
540       pz    -29.622    $xy-plane
640       pz     29.622    $xy-plane
550       pz    -43.562    $xy-plane
650       pz     43.562    $xy-plane
560       pz    -59.244    $xy-plane
660       pz     59.244    $xy-plane
570       pz    -74.926    $xy-plane
670       pz     74.926    $xy-plane
580       pz    -87.123    $xy-plane
680       pz     87.123    $xy-plane

C
C     Material Cards are made of three sets of nubmers
C       (1) Material label corresponding to those in Cell Cards.
C       (2) MCNP library using Z and A atomic numbers.
C       (3) Weight fraction of each isotope.
C       Detector
m1       48000.35C     1      $Cd
C       Shield
m2       5010.60C    -.782610 $B
        12000.60C    -.217390 $C
C       Granite
m3       1001.60C    -.001164 $H
```

```
          6000.60C    -.000218 $C
          8016.60C    -.481577 $O,   no natural O
         11023.60C    -.027820 $Na
         12000.60C    -.010493 $Mg
         13027.60C    -.083251 $Al
         14000.60C    -.308928 $Si
         15031.60C    -.000786 $P
         19000.60C    -.022663 $K
         20000.60C    -.027373 $Ca
         22000.60C    -.003236 $Ti
         25055.60C    -.000620 $Mn
         26056.60C    -.031871 $Fe   no natl Fe
C        Water
m4        1001.60C    -.086073 $H
          8016.60C    -.683158 $O,   no natural O
         11023.60C    -.090779 $Na
         17000.60C    -.139991 $Cl
mt4      lwtr
C     Modes: here both neutron and photon transport are simulated
mode     n p
C
C     Neutron Source Definitions
C       spatial position of neutron source, cell number of source location,
C       energy of source neutrons, bias weight of of source neutrons,
C       starting time for the release of neutrons.
sdef     pos=0 0 4 cel=31 erg=14 wgt=1 tme=0
C
C
C     Tallies: t1, t2, t3, ..., tn. where the tallies are taken from
C       0 to t1, t1 to t2, ..., tn-1 to tn.  tn in units of 10^(-8) sec
t0    1e2 1e3 2e3 3e3 1e38
C
C
fc5   **Photon Tallies**
C       f5 tally:  the first three numbers are the spatial location
C       of the detector.  The last number is the radius of spherical
C       volume over which the average is taken.
f5:p   0.0 0.0 0.0 2.0
C
C     Energy intervals for photon tallies
```

```
C       beginning energy bin in MeV, number of intervals, final energy bin.
e5      0.0 999I 10
C
fc15  **Neutron Tallies**
C       f5 tally for neutrons. The first three numbers are the spatial
C       location of the neutron detector.  The last is the radius of
C       the spherical volume over which the average is taken.
f15:n  0.1 0.0 0.0 0.0
C     Energy intervals for neutron tallies (MeV)
e15     1.26E-10  2.00E-10  3.16E-10  5.01E-10  7.94E-10
        1.26E-09  2.00E-09  3.16E-09  5.01E-09  7.94E-09
        1.26E-08  2.00E-08  3.16E-08  5.01E-08  7.94E-08
        1.26E-07  2.00E-07  3.16E-07  5.01E-07  7.94E-07
        1.26E-06  2.00E-06  3.16E-06  5.01E-06  7.94E-06
        1.26E-05  2.00E-05  3.16E-05  5.01E-05  7.94E-05
        1.26E-04  2.00E-04  3.16E-04  5.01E-04  7.94E-04
        1.26E-03  2.00E-03  3.16E-03  5.01E-03  7.94E-03
        1.26E-02  2.00E-02  3.16E-02  5.01E-02  7.94E-02
        1.26E-01  2.00E-01  3.16E-01  5.01E-01  7.94E-01
        1.26      2.00      3.16      5.01      7.94
        12.6      20
C
C     Number of Source Neutrons
nps       8000000
```

Report Number (14) LBNL--40866

Publ. Date (11) 199801

Sponsor Code (18) DOE/ER, XF

UC Category (19) UC-400, DOE/ER

DOE